Nonlinear Waves over Vortices

Christopher W. Curtis
Henrik Kalisch

1   Introduction

Motivated by the need to identify moving underwater objects by their surface wave signatures, a number of authors have studied the problem of how free fluid surfaces respond to the motion of submerged vortices. This has included detailed analytic studies of one or two vortices for short times [1, 2], and numerical and experimental studies of two vortices over asymptotically significant time scales [3, 4, 5, 6]. Complementing this work, using conformal maps and asymptotic methods, the details of how an isolated vortex over an infinitely deep fluid can induce surface wave radiation up to and past the speed of sound was studied in [7]. This previous work defined two types of vortex pairs, the so-called 'sub-critical' and 'super-critical' cases characterized by the magnitude of the non-dimensional Froude number. In the super-critical case, the vortices move closer together while rising, inducing the formation of a surface hump around the vortices and 'scars', or depressions, on either side of the surface hump. The sub-critical case is characterized by a relatively weak surface response with the vortex motion proceeding as in the case of a rigid lid for long time scales. In either case though, on long enough time scales, breaking occurs when the vortices are close enough to the surface.

However, in this previous work, the fluid is assumed infinitely deep and constraints are explicitly placed on the flow which keep the vortex positions symmetric. Thus bottom boundary effects are not captured, and while there is agreement with experimental results, the symmetry restrictions used in previous simulation and analysis do not allow for the full range of relevant flows. To go further then, in a shallow-water regime, by extending the method of [8], we derive a system of differential-integral equations which describes the surface/point vortex system for an arbitrary number of submerged vortices. Using the Dirichlet-to-Neumann Operator (DNO) approach of [9, 10], we are able to develop long time numerical simulations which capture most if not all of the nonlinear interactions between the surface and the vortices, where again we can have an arbitrary number of vortices. This is a fundamentally different approach than has been used in previous literature.

In order to connect back to previous work, we present results for a counter-rotating vortex pair in the super-critical case. This is done both under a traveling wave and under a quiescent surface. We study several parameter regimes in the case of vortices moving under a traveling wave which allows us to characterize sub and super critical parameter regimes. Likewise, for the case of initially quiescent surface profiles, while we are able to find much of the general phenomena seen previously, we see that waves of higher amplitude form over shorter time scales due to the presence of the bottom boundary which produces an upwelling effect unseen in previous work. This leads to the formation of large amplitude nonlinear waves with deeper scars than previously seen. Ultimately, this appears to lead to wave breaking on much faster time scales.

We then look at several cases of two pairs of vortices with net zero angular momentum. While sharing some similar characteristics with the two vortex case, the added interactions give rise to a wide variety of higher amplitude surface profiles and potential wave-breaking mechanisms that have not been studied. While multi-vortex systems have been looked at in [11], where the canonical Hamiltonian structure of collections of vortices underneath surface waves was derived, the dynamics of multi-vortex systems were not studied. Thus our results are fundamentally new.

The study of larger collections of vortices is motivated by the experiments in [12, 13, 14] which show that surface waves induce eddy formation as they move over varying bathymetry in shallow water. The interaction between eddies and surface waves is not well studied, and as these experiments show, it must be an ubiquitous feature of coastal flows. However, direct simulations of flows with nontrivial vorticity and free surfaces are difficult to develop and difficult to interpret. We advocate instead that by approximating eddies as large collections of irrotational point vortices, the necessary physics can be captured while allowing for the use of far simpler systems of model equations. The work of the present paper is a first step in this direction.

Aside from easing the development of numerical simulations, other effects could be readily included to the present work, such as varying bathymetry, stratification, and constant background shear currents. Further, the framework used in this paper allows for the ready derivation of asymptotic reductions of the full nonlinear system, thus providing further physical insight that would be difficult to obtain from direct simulation alone. By following these future research directions, we can expect to increase our understanding of tsunami propagation and wave-energy device design, and thus the present work should have impact on important applications.

The outline of the paper is as follows. The remainder of this section presents the classic, bulk-variable, dependent model for the surface-wave/vortex system. Section 2 presents the extension to the method in [8] whereby we write model equations in terms of surface variables and vortex positions alone, thus removing any dependence on bulk-variables. Section 3
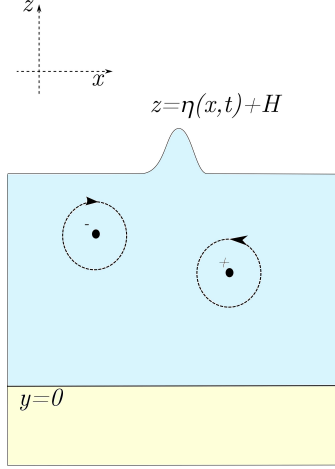
Figure 1: An irrotational point vortex submerged under a free surface gravity wave.

presents the shallow water formulation of the surface-wave/vortex system. DNO expansions and the linearization of the surface -wave/vortex system are derived. Section 4 presents the results of several numerical simulations involving both two and four vortices. Section 5 presents conclusions of this work and also further describes future directions.

1.1 Model Formulation

Throughout this work, we assume the fluid is inviscid and incompressible. We place an impermeable boundary at $z = 0$ and a free surface at $z = \eta(x,t) + H$. The only vorticity in the problem comes from a collection of irrotational point vortices submerged beneath the free surface. We take the fluid domain to be periodic, with period $2L$, and $-L \leq x \leq L$. See Figure 1 for reference.

Given our assumptions on the fluid, the fluid velocity $\mathbf{u}$ is given by the gradient of a potential, say ϕ. We can further separate this potential by writing

$$\phi(x,z,t) = \phi_v(x,z,t) + \tilde{\phi}(x,z,t).$$

The potential $\tilde{\phi}$ describes the bulk and surface fluid flow while the potential describing the vortex motion, ϕ_v, is defined to be

$$\phi_v(x,z,t) = \frac{1}{2\pi} \sum_{j=1}^{N} \Gamma_j \phi_{v,j}(x,z,t), \tag{1}$$

with Γ_j denoting the circulation strength of the vortices and

$$\phi_{v,j}(x,z,t) = \phi_{v,j}^{+}(x,z,t) - \phi_{v,j}^{-}(x,z,t),$$

3

where, denoting the vortex positions as $\mathbf{x}_j(t) = (x_j(t), z_j(t))$, we set

$$\phi_{v,j}^+(x, z, t) = \Phi_p(x - x_j(t), z - z_j(t)), \ \phi_{v,j}^-(x, z, t) = \Phi_p(x - x_j(t), z + z_j(t)),$$

where

$$\Phi_p(x, z) = \sum_{m=-\infty}^{\infty} \tan^{-1}\left(\frac{z}{x - 2mL}\right).$$

Our choice for ϕ_v, aside from addressing the requirement of periodic boundary conditions, ensures that

$$\partial_z \phi_v|_{z=0} = 0.$$

By further supposing that

$$\partial_z \tilde{\phi}\Big|_{z=0} = 0,$$

we satisfy the assumption that $z = 0$ is an impermeable boundary.

While we should think of the sum defining ϕ_v formally, this is not the case for its derivatives, which ultimately define the physically meaningful fluid velocity. Using Fourier transform arguments, one can show that

$$\sum_{m=-\infty}^{\infty} \frac{s}{(t - 2m\pi)^2 + s^2} = \frac{\sinh(s)}{2(\cosh(s) - \cos(t))}$$

and

$$\sum_{m=-\infty}^{\infty} \frac{t - 2m\pi}{(t - 2m\pi)^2 + s^2} = \frac{\sin(t)}{2(\cosh(s) - \cos(t))}$$

Standard arguments then give for the vortex velocities

$$\dot{x}_j = \frac{1}{4L}\left(\Gamma_j \coth\left(\frac{\pi z_j}{L}\right) + 2\sum_{l\neq j}\Gamma_l v_{jl}^{(h)}\right) + \tilde{\phi}_x(x_j, z_j, t), \tag{2}$$

$$\dot{z}_j = \frac{1}{2L}\sinh\left(\frac{\pi}{L}z_j\right)\sum_{l\neq j}\Gamma_l v_{jl}^{(v)} + \tilde{\phi}_z(x_j, z_j, t), \tag{3}$$

where

$$v_{jl}^{(h)} = \frac{\sinh\left(\frac{\pi}{L}z_l\right)\left(\cosh(\frac{\pi}{L}z_l) - \cosh(\frac{\pi}{L}z_j)\cos\left(\frac{\pi}{L}(x_j - x_l)\right)\right)}{\left(\cosh\left(\frac{\pi}{L}(z_j - z_l)\right) - \cos\left(\frac{\pi}{L}(x_j - x_l)\right)\right)\left(\cosh\left(\frac{\pi}{L}(z_j + z_l)\right) - \cos\left(\frac{\pi}{L}(x_j - x_l)\right)\right)},$$

$$v_{jl}^{(v)} = \frac{\sin\left(\frac{\pi}{L}(x_j - x_l)\right)\sinh\left(\frac{\pi}{L}z_l\right)}{\left(\cosh\left(\frac{\pi}{L}(z_j - z_l)\right) - \cos\left(\frac{\pi}{L}(x_j - x_l)\right)\right)\left(\cosh\left(\frac{\pi}{L}(z_j + z_l)\right) - \cos\left(\frac{\pi}{L}(x_j - x_l)\right)\right)}.$$

At the surface, we have the kinematic condition which, separating into vortex and bulk variables becomes

$$\eta_t - \tilde{\phi}_z + \eta_x \tilde{\phi}_x = P_v(x, \eta, t), \ z = \eta(x, t) + H, \tag{4}$$

4

where

$$P_v(x, \eta, t) = \partial_z \phi_v - \eta_x \partial_x \phi_v.$$

Finally, at the surface, we have the Bernoulli equation, which becomes after separating into vortex and bulk variables

$$\tilde{\phi}_t + \frac{1}{2} \left| \nabla \tilde{\phi} \right|^2 + \nabla \phi_v \cdot \nabla \tilde{\phi} + g\eta = E_v(x, \eta, t), \tag{5}$$

where

$$E_v(x, \eta, t) = \frac{1}{2\pi} \sum_{j=1}^{N} \Gamma_j \left(\dot{x}_j \partial_x \phi_{v,j} + \dot{z}_j \partial_z \left(\phi_{v,j}^+ + \phi_{v,j}^- \right) \right) - \frac{1}{2} \left| \nabla \phi_v \right|^2.$$

The system given by Equations (2)-(5) coupled with the bulk requirement that

$$\Delta \tilde{\phi} = 0, \ 0 \le z \le \eta(x, t) + H, \tag{6}$$

and the Neumann boundary condition $\partial_z \tilde{\phi}(x, 0, t) = 0$, gives a closed system of equations in terms of η, $\tilde{\phi}$, and the vortex positions $(x_j(t), z_j(t))$. However, this requires the solution of a nonlinear free boundary value problem, which does not allow for any direct analytic solution approaches. Further, even with regards to developing numerical schemes, anything which removes the need to solve throughout the bulk of the fluid is desirable.

We can partially achieve this goal. Defining

$$\tilde{q}(x, t) = \tilde{\phi}(x, \eta(x, t) + H, t),$$

we can transform the derivatives of the potential at the surface via the equations

$$\begin{pmatrix} \tilde{\phi}_x \\ \tilde{\phi}_z \end{pmatrix} \bigg|_{z=\eta+H} = \frac{1}{1 + \eta_x^2} \begin{pmatrix} 1 & \eta_x \\ \eta_x & -1 \end{pmatrix} \begin{pmatrix} \tilde{q}_x \\ -\eta_t + P_v \end{pmatrix}, \tag{7}$$

and

$$\tilde{\phi}_t = \tilde{q}_t - \tilde{\phi}_z \eta_t, \tag{8}$$

and therefore rewrite the Bernoulli equation (5) in terms of surface variables and vortex positions alone. However, since we have made use of the kinematic condition Equation (4), we cannot rewrite this equation in terms of itself. Likewise, we have no means of removing the bulk-variable dependence in Equations (2) and (3).

To address this issue, we now turn to the method of Ablowitz, Fokas, and Mussilimani (AFM) as described in [8]. Through an extension to the existing scheme, we will be able to write a closed system of equations in terms of surface variables and vortex positions alone. This will remove any need to solve equations, either analytically or numerically, throughout the bulk of the fluid. As we show, this approach then readily allows us to derive efficient numerical approximation schemes.

2 The Surface-Variable/Vortex-Position Formulation

We now show how to rewrite the system of equations (2)-(6) in terms of surface variables and vortex positions alone via the method described in [8]. Making use of Equation (4), the work in [8] readily allows us to rewrite the kinematic condition as the infinite system of integro-differential equations

$$\int_{-L}^{L} e^{-i\pi kx/L} \left(\cosh(k(\eta + H)) \left(\eta_t - P_v\right) + i\tilde{q}_x \sinh(k(\eta + H))\right) dx = 0, \quad (9)$$

for $k \in \mathbb{Z} \backslash \{0\}$. We omit the details of this derivation since one may directly follow the arguments in [8] to derive (9).

Looking at Equations (2) and (3) though, we are still left with needing to evaluate the background flow potential $\tilde{\phi}$ at the vortex positions (x_j, z_j). To deal with this, we introduce the auxillary harmonic functions

$$\psi_{M,j}(x, z, t) = -\frac{1}{4\pi} \sum_{m=-M}^{M} \left(\ln\left(\tilde{x}_{j,m}^2 + \tilde{z}_{j,-}^2\right) + \ln\left(\tilde{x}_{j,m}^2 + \tilde{z}_{j,+}^2\right)\right).$$

where

$$\tilde{x}_{j,m} = \frac{(x - x_j - 2mL)}{L}, \ \tilde{z}_{j,-} = \frac{\gamma}{H}(z - z_j), \ \tilde{z}_{j,+} = \frac{\gamma}{H}(z + z_j),$$

and

$$\gamma = \frac{H}{L}.$$

Our choice of auxillary harmonic function ensures that $\partial_z \psi_{M,j}(x, 0, t) = 0$. Taking D to be the fluid domain, using Green's third identity, we have that

$$\tilde{\phi}_x(x_j, z_j, t) = \oint_{\partial D} \left(\psi_{M,j} \partial_{\hat{\mathbf{n}}} \tilde{\phi}_x - \tilde{\phi}_x \partial_{\hat{\mathbf{n}}} \psi_{M,j}\right) ds,$$

where $\hat{\mathbf{n}}$ is an outward pointing unit normal vector along the path ∂D_ϵ. Note, if $\tilde{\phi}$ is harmonic, then so are all of its partial derivatives. Defining

$$g_M(x, z, t) = \psi_{M,j} \partial_{\hat{\mathbf{n}}} \tilde{\phi}_x - \tilde{\phi}_x \partial_{\hat{\mathbf{n}}} \psi_{M,j},$$

We can then decompose the line integral such that

$$\oint_{\partial D} g_M(x, z, t) ds = \int_{-L}^{L} g_M(x, \eta(x, t) + H, t)(1 + \eta_x^2)^{1/2} dx$$
$$+ \int_{0}^{\eta(L,t)+H} \left(g_M(L, z, t) + g_M(-L, z, t)\right) dz.$$

We now look at letting $M \to \infty$. As defined, $\psi_{M,j}$ does not have a well defined limit, however, its derivatives are well defined in this limit, and as we

show, it is well behaved along boundaries. To see this, along $z = \eta(x,t) + H$, we have that

$$g_M(1+\eta_x^2)^{1/2} = \left(\psi_{M,j}\left(-\eta_x\tilde{\phi}_{xx} + \tilde{\phi}_{xz}\right) - \tilde{\phi}_x\left(-\eta_x\partial_x\psi_{M,j} + \partial_z\psi_{M,j}\right)\right)\Big|_{z=\eta+H}.$$

Using $\tilde{\phi}_{xx} = -\tilde{\phi}_{zz}$, we get the identity

$$\partial_x\left(\tilde{\phi}_z(x, \eta + H, t)\right) = -\eta_x\tilde{\phi}_{xx} + \tilde{\phi}_{xz}.$$

Thus, by integration by parts and using the fact that $\tilde{\phi}(x,z,t)$ and its derivatives are assumed to be periodic in x, we have that

$$\int_{-L}^{L} g_M(x, \eta(x,t) + H, t)(1 + \eta_x^2)^{1/2}dx = -\int_{-L}^{L}\left(\tilde{\phi}_z\psi_{M,j}^{(1)} + \tilde{\phi}_x\psi_{M,j}^{(2)}\right)\Big|_{z=\eta+H}dx$$
$$+ \tilde{\phi}_z(L, \eta + H, t)\psi_{M,j}^{(\delta)}(\eta + H, t),$$

where

$$\psi_{M,j}^{(1)}(x,t) = \partial_x\psi_{M,j} + \eta_x\partial_z\psi_{M,j}|_{z=\eta+H},$$
$$\psi_{M,j}^{(2)}(x,t) = -\eta_x\partial_x\psi_{M,j} + \partial_z\psi_{M,j}|_{z=\eta+H},$$
$$\psi_{M,j}^{(\delta)}(z,t) = \psi_{M,j}(L, z, t) - \psi_{M,j}(-L, z, t).$$

Likewise, we have that

$$\int_0^{\eta(L,t)+H}\left(g_M(L, z, t) + g_M(-L, z, t)\right)dz = \int_0^{\eta(L,t)+H}\left(\tilde{\phi}_{xx}(L, z, t)\psi_{M,j}^{(\delta)}(z,t)\right.$$
$$\left. + \tilde{\phi}_x(L, z, t)\psi_{M,j}^{(\delta,x)}(z,t)\right)dz,$$

where

$$\psi_{M,j}^{(\delta,x)}(z,t) = \partial_x\psi_{M,j}(L, z, t) - \partial_x\psi_{M,j}(-L, z, t).$$

One can readily show that

$$\psi_{M,j}^{(\delta)} = \frac{1}{4\pi}\ln\left(\left(\frac{(1 - \tilde{x}_j - 2M)^2 + \tilde{z}_{j,-}^2}{(1 - \tilde{x}_j + 2(M+1))^2 + \tilde{z}_{j,-}^2}\right)\left(\frac{(1 - \tilde{x}_j - 2M)^2 + \tilde{z}_{j,+}^2}{(1 - \tilde{x}_j + 2(M+1))^2 + \tilde{z}_{j,+}^2}\right)\right),$$

where

$$\tilde{x}_j = \frac{x_j}{L},$$

and thus

$$\lim_{M\to\infty}\psi_{M,j}^{(\delta)}(z,t) = 0.$$

Letting $M \to \infty$, we then have

$$\tilde{\phi}_x(x_j, z_j, t) = -\int_{-L}^{L}\left(\tilde{\phi}_z\left(\partial_x\psi_j + \eta_x\partial_z\psi_j\right) + \tilde{\phi}_x\left(-\eta_x\partial_x\psi_j + \partial_z\psi_j\right)\right)\Big|_{z=\eta+H}dx,$$

7

where we define the functions $\partial_x\psi_j$ and $\partial_z\psi_j$ such that

$$\partial_x\psi_j(x,z,t) = \lim_{M\to\infty} \partial_x\psi_{M,j}(x,z,t),$$
$$\partial_z\psi_j(x,z,t) = \lim_{M\to\infty} \partial_z\psi_{M,j}(x,z,t).$$

Transforming to surface variables using Equation (7) then gives

$$\tilde{\phi}_x(x_j,z_j,t) = -\int_{-L}^{L} \left.\left((\eta_t - P_v)\,\partial_x\psi_j + \tilde{q}_x\partial_z\psi_j\right)\right|_{z=\eta+H} dx.$$

Proceeding in a similar fashion for $\tilde{\phi}_z$, we introduce the auxillary harmonic function

$$\tilde{\psi}_j = -\frac{1}{4\pi} \sum_{m=-\infty}^{\infty} \left(\ln\left(\tilde{x}_{j,m}^2 + \tilde{z}_{j,-}^2\right) - \ln\left(\tilde{x}_{j,m}^2 + \tilde{z}_{j,+}^2\right)\right).$$

This choice ensures that $\tilde{\psi}_j(x,0,t) = 0$. Using the arguments from above, we then can find that

$$\tilde{\phi}_z(x_j,z_j,t) = -\int_{-L}^{L} \left.\left(\tilde{\psi}_j\left(\eta_x\tilde{\phi}_{xz} + \tilde{\phi}_{xx}\right) + \tilde{\phi}_z\left(-\eta_x\partial_x\tilde{\psi}_j + \partial_z\tilde{\psi}_j\right)\right)\right|_{z=\eta+H} dx,$$

where we have used the fact that $\tilde{\phi}_{zz} = -\tilde{\phi}_{xx}$. Integrating by parts then gives

$$\tilde{\phi}_z(x_j,z_j,t) = -\int_{-L}^{L} \left.\left(-\tilde{\phi}_x\left(\partial_x\tilde{\psi}_j + \eta_x\partial_z\tilde{\psi}_j\right) + \tilde{\phi}_z\left(-\eta_x\partial_x\tilde{\psi}_j + \partial_z\tilde{\psi}_j\right)\right)\right|_{z=\eta+H} dx,$$

which can be shown, again using Equation (7), to yield

$$\tilde{\phi}_z(x_j,z_j,t) = -\int_{-L}^{L} \left.\left((\eta_t - P_v)\,\partial_z\tilde{\psi}_j - \tilde{q}_x\partial_x\tilde{\psi}_j\right)\right|_{z=\eta+H} dx.$$

Thus, we have now shown how to rewrite Equations (2) and (3) in the bulk-independent form

$$\dot{x}_j = \frac{1}{4L}\left(\Gamma_j\mathrm{cotanh}\left(\frac{\pi z_j}{L}\right) + 2\sum_{l\neq j}\Gamma_l v_{jl}^{(h)}\right)$$
$$\quad - \int_{-L}^{L} \left.\left((\eta_t - P_v)\,\partial_x\psi_j + \tilde{q}_x\partial_z\psi_j\right)\right|_{z=\eta+H} dx, \tag{10}$$
$$\dot{z}_j = \frac{1}{2L}\sinh\left(\frac{\pi}{L}z_j\right)\sum_{l\neq j}\Gamma_l v_{jl}^{(v)}$$
$$\quad - \int_{-L}^{L} \left.\left((\eta_t - P_v)\,\partial_z\tilde{\psi}_j - \tilde{q}_x\partial_x\tilde{\psi}_j\right)\right|_{z=\eta+H} dx. \tag{11}$$

Thus, coupled with the use of (7) to rewrite (5), and the use of the AFM method to derive (9), we have now derived a system of equations that are in terms of surface variables and vortex positions alone. The approach outlined above complements those used for particle tracing in [15] and [16].

3 Shallow Water Theory: Scalings and Linear Dynamics

We now choose the following non-dimesionalizations

$$\tilde{x} = \frac{x}{L}, \ \tilde{z} = \frac{z}{H}, \ \tilde{t} = \frac{\sqrt{gH}}{L}t, \ \eta = d\tilde{\eta}, \ \tilde{\phi} = \mu L\sqrt{gH}\tilde{\tilde{\phi}},$$

where we define the non-dimensional parameters

$$\mu = \frac{d}{H}, \ \gamma = \frac{H}{L},$$

and where we define the Froude number F to be

$$F = \frac{\Gamma}{\mu L\sqrt{gH}}.$$

If we then define $Q = \tilde{q}_x$, the Bernoulli equation (5) becomes, after using Equations (7) and (8) and then dropping tildes,

$$Q_t + \eta_x + \mu\partial_x \frac{1}{1 + \mu^2\gamma^2\eta_x^2} \left(\frac{1}{2}Q^2 - \mu\gamma^2\eta_t\eta_x Q + \phi_{sx}(Q + \mu\gamma\eta_x(P_s - \gamma\eta_t)) \right.$$
$$\left. + \frac{1}{2}\left(P_s^2 - \gamma^2\eta_t^2\right) + \phi_{sz}\left(\gamma\mu\eta_x Q - (P_s - \gamma\eta_t)\right) \right) = \partial_x E_s(x,t). \tag{12}$$

The associated vortex position dependent functions in Equation (12) are given by

$$\phi_{sz}(x,t) = F\sum_{j=1}^{N}\Gamma_j\varphi_z(x - x_j, 1 + \mu\eta; z_j),$$

$$\phi_{sx}(x,t) = F\sum_{j=1}^{N}\Gamma_j\varphi_x(x - x_j, 1 + \mu\eta; z_j),$$

$$P_s(x,t) = \phi_{sz}(x,t) - \mu\gamma\eta_x\phi_{sx}(x,t),$$

$$E_s(x,t) = F\sum_{j=1}^{N}\Gamma_j\left(\dot{x}_j\varphi_x(x - x_j, 1 + \mu\eta; z_j) + \gamma\dot{z}_j\tilde{\varphi}_z(x - x_j, 1 + \mu\eta; z_j)\right)$$
$$- \frac{\mu}{2}\left(\phi_{sx}^2 + \phi_{sz}^2\right).$$

where

$$\varphi_z(x, z; z_j) = \frac{\sin(\pi x)\sinh(\pi\gamma z)\sinh(\pi\gamma z_j)}{2\left(\cosh(\pi\gamma(z - z_j)) - \cos(\pi x)\right)\left(\cosh(\pi\gamma(z + z_j)) - \cos(\pi x)\right)},$$

$$\tilde{\varphi}_z(x,z;z_j) = \frac{\sin(\pi x)\left(\cosh(\pi\gamma z_j)\cosh(\pi\gamma z) - \cos(\pi x)\right)}{2\left(\cosh(\pi\gamma(z-z_j)) - \cos(\pi x)\right)\left(\cosh(\pi\gamma(z+z_j)) - \cos(\pi x)\right)},$$

$$\varphi_x(x,z;z_j) = \frac{\sinh(\pi\gamma z_j)\left(\cosh(\pi\gamma z_j) - \cosh(\pi\gamma z)\cos(\pi x)\right)}{2\left(\cosh(\pi\gamma(z-z_j)) - \cos(\pi x)\right)\left(\cosh(\pi\gamma(z+z_j)) - \cos(\pi x)\right)}.$$

The AFM equation (9) becomes

$$\int_{-1}^{1} e^{-i\pi kx}\left(\cosh\left(\pi\gamma k(1+\mu\eta)\right)\left(\eta_t - \frac{1}{\gamma}P_v(x, 1+\mu\eta, t)\right)\right.$$
$$\left. +i\frac{1}{\gamma}Q\sinh\left(\pi\gamma k(1+\mu\eta)\right)\right)dx = 0, \ k \in \mathbb{Z}, \qquad (13)$$

and Equations (10) and (11) become

$$\dot{x}_j = \frac{F\mu}{4}\left(\Gamma_j \cotanh(\pi\gamma z_j) + 2\sum_{l\neq j}\Gamma_l v_{jl}^{(h)}\right) + \qquad (14)$$
$$\mu\int_{-1}^{1}\left((\gamma\eta_t - P_s)\tilde{\varphi}_z(x-x_j, z; z_j) + Q\tilde{\varphi}_x(x-x_j, z; z_j)\right)|_{z=1+\mu\eta}\, dx,$$

$$\dot{z}_j = \frac{F\mu}{2\gamma}\sinh(\pi\gamma z_j)\sum_{l\neq j}\Gamma_l v_{jl}^{(v)} - \qquad (15)$$
$$\frac{\mu}{\gamma}\int_{-1}^{1}\left((\gamma\eta_t - P_s)\varphi_x(x-x_j, z; z_j) + Q\varphi_z(x-x_j, z; z_j)\right)|_{z=1+\mu\eta}\, dx,$$

where

$$\tilde{\varphi}_x(x,z;z_j) = \frac{\sinh(\pi\gamma z)(\cosh(\pi\gamma z) - \cosh(\pi\gamma z_j)\cos(\pi x))}{2(\cosh(\pi\gamma(z-z_j)) - \cos(\pi x))(\cosh(\pi\gamma(z+z_j)) - \cos(\pi x))}.$$

We now develop the machinery necessary to implement numerical schemes to solve the system of equations (12), (13), (14), and (15).

3.1 Dirichlet-to-Neumann Expansions

Our choice of scaling allows us to readily generate the Dirichlet-to-Nuemann Operator (DNO) expansion. This is done, as in [9] and elsewhere, by supposing that

$$\eta_t - \frac{1}{\gamma}P_v(x, 1+\mu\eta, t) = \left(G_0 + \mu G_1 + \mu^2 G_2 + \cdots\right)Q.$$

Defining the Fourier transform of a periodic function $f(x)$ to be $\hat{f}$, so that

$$\hat{f}(k) = \frac{1}{2}\int_{-1}^{1}f(x)e^{-i\pi kx}dx, \ k \in \mathbb{Z},$$

we define, for a linear operator L, its associated symbol $\hat{L}(k)$ by way of the formula

$$\hat{L}(k)\hat{f}(k) = \frac{1}{2}\int_{-1}^{1} Lf(x)e^{-i\pi kx}dx.$$

Using the AFM equation (13), we then get

$$\hat{G}_0(k) = -\frac{i}{\gamma}\tanh(\pi\gamma k),$$

and, for $m \geq 1$,

$$G_m Q = -\sum_{j=1}^{\lfloor m/2 \rfloor} \frac{1}{(2j)!}D_\gamma^{2j}\left(\eta^{2j}G_{m-2j}Q\right)$$

$$-\gamma^2\partial_x G_0 \sum_{j=0}^{\lfloor (m-1)/2 \rfloor} \frac{D_\gamma^{2j}}{(2j+1)!}\left(\eta^{2j+1}G_{m-2j-1}Q\right) - \frac{1}{m!}L_m\partial_x D_\gamma^{m-1}\left(\eta^m Q\right),$$

where

$$\hat{D}_\gamma = \pi\gamma k,$$

and

$$\hat{L}_m = \begin{cases} 1, & m \text{ is odd,} \\ i\gamma\hat{G}_0(k), & m \text{ is even.} \end{cases}$$

3.2   Linear Dynamics

In order to get at least some short time intuition about the response of the above system, we suppose that $\mu \ll \gamma$, so that in the linear regime we have $\dot{x}_j \sim 0$, $\dot{z}_j \sim 0$,

$$Q_t + \eta_x = 0,$$

and

$$\hat{\eta}_t - \hat{G}_0(k)\hat{Q} = F\int_{\mathbb{R}} e^{-i\pi kx}\tilde{P}_v dx,$$

where

$$\tilde{P}_v = \frac{\gamma\sqrt{2}}{\pi}\sum_{j=1}^{n}\Gamma_j z_j e^{-i\pi kx_j}\frac{x}{(x^2 + \gamma^2(1-z_j)^2)(x^2 + \gamma^2(1+z_j)^2)}.$$

We can readily show using a contour integral argument that

$$\int_{\mathbb{R}} e^{-i\pi kx}\tilde{P}_v dx = -\frac{i}{\sqrt{2}}\sum_{j=1}^{n}\Gamma_j\frac{\sinh(\pi\gamma k z_j)}{\gamma}e^{-i\pi kx_j - \pi\gamma|k|}.$$

Note, in order for this result to hold, we need to assume that $0 \leq z_j < 1$. Thus, if we linearize around a quiescent initial condition, using (1) whereby we have

$$\hat{\eta}(k, 0) = 0, \ \hat{Q}(k, 0) = \hat{Q}_0(k) = -ik\hat{\phi}_v(k, 1)$$

in frequency space, we get the leading order behavior

$$
\begin{pmatrix} \hat{Q}(k,t) \\ \hat{\eta}(k,t) \end{pmatrix} = \hat{Q}_0(k) \begin{pmatrix} \cos(\omega(k)t) \\ \frac{\omega}{i\pi k}\sin(\omega(k)t) \end{pmatrix}
$$
$$
- \frac{iF}{\sqrt{2}} \begin{pmatrix} i\pi k(\cos(\omega(k)t)-1)/\omega(k) \\ \sin(\omega(k)t) \end{pmatrix} \sum_{j=1}^{n} \Gamma_j \frac{\sinh(\pi\gamma k z_j)}{\gamma\omega(k)} e^{-i\pi k x_j - \pi\gamma|k|},
$$

where

$$
\omega(k) = \sqrt{\frac{\pi k \tanh(\pi\gamma k)}{\gamma}}.
$$

Defining the surface response to the vortex induced forcing as $R_s(x,t)$, we readily see that this is given by

$$
R_s(x,t) = F \sum_{j=1}^{n} \Gamma_j R_{s,j}(x,t).
$$

where the functions $R_{s,j}$ are found by taking inverse Fourier transforms and using symmetry arguments such that one finds

$$
R_{s,j}(x,t) = \sum_{k=1}^{\infty} \frac{\sin(\omega(k)t)}{\omega(k)} \frac{\sinh(\pi\gamma k z_j)}{\gamma} e^{-\pi\gamma k} \sin(\pi k(x-x_j)).
$$

4 Numerical Results

For all of the following simulations, we use a pseudo-spectral in space and fourth order Runge-Kutta in time method of lines, and choose $\mu = .2$ and $\gamma = \sqrt{\mu}$. The domain is sampled with $K_M = 256$ modes giving a grid spacing of $\delta x = 1/128$, while the time step used is $\delta t = 1 \times 10^{-2}$, which introduces error on the order of 10^{-8}. The Orszag "2/3-rule" is used to control aliasing error throughout the simulation.

For those problems involving only two vortices, we use the initial positions
$$
x_1(0) = -\mu\gamma, \ x_2(0) = \mu\gamma, \ z_1(0) = z_2(0) = .25.
$$
This is done since $d/L = \mu\gamma$, and thus these initial positions are consistent with our scaling assumptions. For those problems involving four vortices, we set

$$
x_1(0) = -2\mu\gamma - \mu\gamma/2, \ x_2(0) = -2\mu\gamma + \mu\gamma/2,
$$
$$
x_3(0) = 2\mu\gamma - \mu\gamma/2, \ x_4(0) = 2\mu\gamma + \mu\gamma/2,
$$

and $z_j(0) = .25$. Throughout, we keep $|\Gamma_j| = 1$ and use the Froude number F to set the effective strength of the vortices.

It is nontrivial at this point to describe what choices of F correspond to subcritical or supercritical vortices as described in the previous literature. We note that our choice of F is not the same as in for example [1] or [5], where they define the Froude number $\tilde{F}$ to be

$$\tilde{F} = \frac{\Gamma}{d^{3/2}g^{1/2}}.$$

Comparing these two choices of Froude number shows our choice for F satisfies the equation

$$F = \gamma\sqrt{\mu}\tilde{F}.$$

The supercritical or strong case is usually taken to be when $\tilde{F} \geq 1$, which corresponds to $F \geq .2$ using the values for μ and γ from above. However, the distinction between sub and supercritical is better defined by phenomena, whereby in the subcritical case, the motion of surface waves has a strong influence on vortex motion, and in the supercritical case, the vortex motion drives surface wave dynamics. Thus, throughout most of the simulations, we choose $F = .2$, but we take care to try to describe the relative strength of the vortex system based on the observed dynamics.

For each simulation, there is of course the question of where to truncate the DNO expansions. We use the convention of taking enough terms, say $\tilde{N}$, such that, using the numerically computed solution for $Q(x, t_f)$, where t_f is the final time a given simulation is run to, we satisfy the criteria

$$\frac{||G_{\tilde{N}}Q||_2}{||Q||_2} \leq \text{eps},$$

where eps denotes machine precision, which on 64-bit machines is on the order of 10^{-16}. We argue that satisfying this inequality should in most cases imply subsequent terms should have little to no effect on the dynamics. However, throughout each simulation, multiple truncation points were chosen to see what impact they had on dynamics, and in all cases, no effect was seen by including terms beyond what would be selected via our truncation convention.

This argument though of course relies on the choice of t_f. Throughout each simulation, t_f is chosen to be long enough so that nonlinear effects can become asymptotically significant, but not long enough so that arbitrarily high-frequency effects dominate the dynamics. As each simulation shows, and as we would expect, these high-frequency modes are due to vortices getting closer to the free surface. We can think of the corresponding high-frequency phenomena as a loss in regularity of the surface profile, which is to say that the surface profile is starting to break. This is a heuristic measurement, and more sophisticated simulations, such as vortex sheet based methods [5, 17], would need to be done to establish at what times vertical gradients or singularities in the wave profile formed. That breaking could

occur is not surprising, and breaking has been observed in the deep water simulations reported on previously [4].

To get some quantitative understanding of when breaking might occur, and to get a better understanding of how moving vortices impart energy into the surface, we include plots of the surface energy $E(t)$ defined to be

$$E(t) = \frac{1}{2}\int_{-1}^{1} qG(\eta)Q\,dx + \frac{1}{2}\int_{-1}^{1}\eta^2 dx.$$

We again note that $Q = q_x$, and our use of Q implies that the form of the DNO G is different than that found in for example [9]. As shown in [11], the surface-wave/vortex system is Hamiltonian with total energy given by $E(t)$ and the energy possessed by the vortices themselves. Thus $E(t)$ provides a direct measurement of the balance between the energy in the surface and the vortices, and we use the dynamics of $E(t)$ to describe when we think breaking phenomena begins to occur.

4.1 Two Counter Propagating Vortices under a Traveling Wave

By setting the vortex strengths, or taking the Froude number F to zero, we would expect to limit onto the classical case of shallow water flow in which the KdV equation becomes a valid asymptotic approximation. Expanding up to $\mathcal{O}(\mu, \gamma^2)$ we get the system of equations

$$\tilde{Q}_t + \eta_x + \frac{\mu}{2}\partial_x Q^2 \sim 0,$$

and

$$\left(1 - \frac{\gamma^2}{2}\partial_x^2\right)\eta_t + \partial_x\left(1 - \frac{\gamma^2}{6}\partial_x^2\right)Q + \mu\partial_x(\eta Q) \sim 0.$$

By introducing the coordinates

$$\xi = x - t, \ \tau = \mu t,$$

and taking the balance

$$\mu = \gamma^2,$$

we derive the Korteweg-de Vries (KdV) equation

$$2Q_\tau + 3QQ_\xi + \frac{1}{3}Q_{\xi\xi\xi} = 0.$$

Note, we see by deriving this equation that we are in fact, in the abscence of vortices, in a classicaly defined shallow water regime, thus justifying our choice of scalings *a posteori*.

As is known, the KdV equation has an infinite number of periodic traveling wave solutions of the form

$$Q(x,t) \sim \frac{2}{3}q_0 + \frac{4}{3}\tilde{m}^2\mathcal{K}^2(\tilde{m})\text{cn}^2\left(\mathcal{K}(\tilde{m})\left(x - (1 + \mu\tilde{c})t\right); \tilde{m}\right),$$

where

$$\tilde{c} = \frac{2}{3}\mathcal{K}^2(\tilde{m})(2\tilde{m}^2 - 1) + q_0,$$

and where $0 \leq \tilde{m} < 1$ is the elliptic modulus of the cnoidal function $\text{cn}(\cdot; \tilde{m})$ and where $\mathcal{K}(\tilde{m})$ represents the complete elliptic integral of the first kind. This then implies that the surface profile is to leading order given by

$$\eta(x,t) \sim \left(1 + \frac{2}{3}\mu\mathcal{K}^2(\tilde{m})(2\tilde{m}^2 - 1)\right)Q(x,t).$$

We then choose $q_0 = 0$ so that as $\tilde{m} \to 1$, we limit onto the classical one-soliton solution of the KdV equation.

Choosing the elliptic modulus to be $\tilde{m} = .2$, we look at the case of two counter-propagating vortices under the traveling wave where we compare the dynamics for $F = 0, .02$, and $.2$. In all cases, we truncate the DNO expansion at the 32nd term, i.e. G_{31}. We run each simulation up to $t = 5 = 1/\mu$ so that nonlinear effects have time to become asymptotically significant.

We note that the case $F = 0$ is equivalent to setting the vortex strengths to zero and thus represents the path of passive tracers in the bulk of the fluid. As can be seen then from the motion of the vortices in Figures 2 and 3, there is very little difference in the vortex paths for $F = .02$ than for that of a passive tracer. Likewise, observing the surface response seen in Figure 4, we see the vortex motion has little to no effect on the surface wave profile. Thus, we can readily argue that the choice of $F = .02$ corresponds to a sub-critical value of the Froude number. In contrast, the choice of $F = .2$ clearly corresponds to a super-critical choice. This can be seen in the stronger vortex dynamics in Figures 2 and 3 as well as the significant impact the vortices have on the surface profile in Figure 5 which induces significant deformations of the original cnoidal profile.

4.2   Two Counter Propagating Vortices Under an Initially Quiescent Surface

Throughout the remainder of the paper, use the initial conditions

$$\eta(x,0) = 0, \ Q(x,0) = -\partial_x\phi_v(x,1),$$

so that the initial surface profile is flat and still. We likewise set $F = .2$ throughout the remainder of the paper.

We first look at the surface response up to $t = .5$. Given the relatively short time scale, we compare our numerics to the linear theory derived in
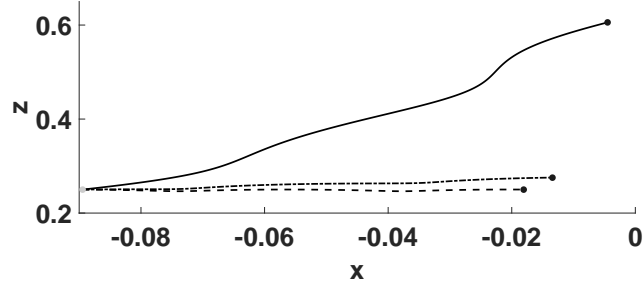
Figure 2: Paths of the left-side vortex moving under a cnoidal wave for $0 \leq t \leq 5$ for Froude numbers $F = 0$ (dashed line), .02 (dashed/dotted line), and .2 (solid line). The vortex motion starts at the light grey dot and ends at the black dot.
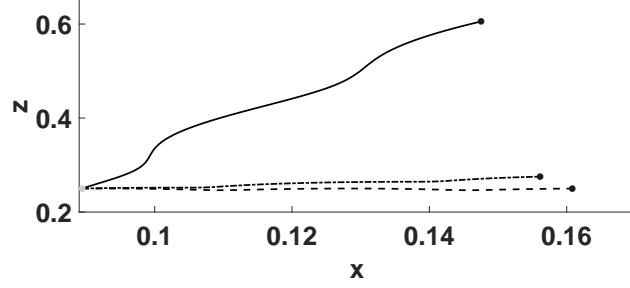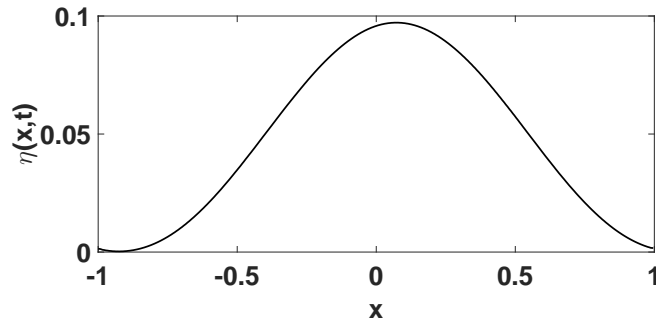

Figure 3: Paths of the right-side vortex moving under a cnoidal wave for $0 \leq t \leq 5$ for Froude numbers $F = 0$ (dashed line), .02 (dashed/dotted line), and .2 (solid line). The vortex motion starts at the light grey dot and ends at the black dot.

Figure 4: Surface response $\eta(x, 5)$ for a traveling cnoidal solution of the KdV equation with elliptic modulus $\tilde{m} = .2$ and Froude number $F = .02$.

the previous section. For a pair of counter-rotating vortices, we have that
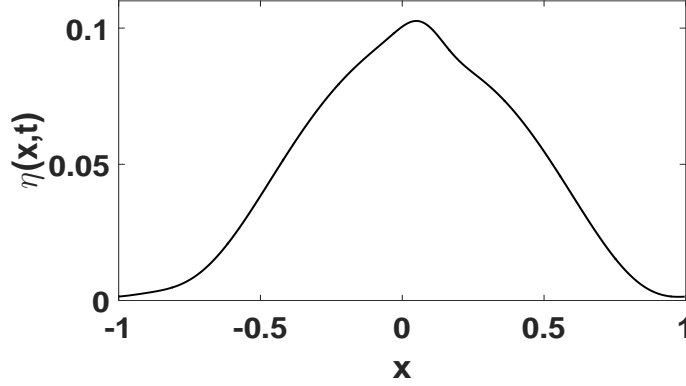
Figure 5: Surface response $\eta(x, 5)$ for a traveling cnoidal solution of the KdV equation with elliptic modulus $\tilde{m} = .2$ and Froude number $F = .2$.

the forcing response for the free surface is given by the function

$$R_s(x, t) = 2\sum_{k=1}^{\infty} \frac{\sin(\omega(k)t)}{\omega(k)} \frac{\sinh(\pi\gamma k z_1)}{\gamma} e^{-\pi\gamma k} \sin(\pi k x_1) \cos(\pi k x).$$

We compare this response function to the numerical results in Figure 6. As can be seen, even up to $t = .5$, the linear response is quite accurate. Further, the falling troughs, or scars, seen in much of the existing literature [4, 6] are present. However, we note that in previous work, the formation of mounds in the surface profile corresponded to the vortices being near the wave crest. Thus, the presence of the bottom boundary and the concomitant upwelling it induces causes wave profiles to form at far shorter time scales and for different reasons than reported in previous literature.
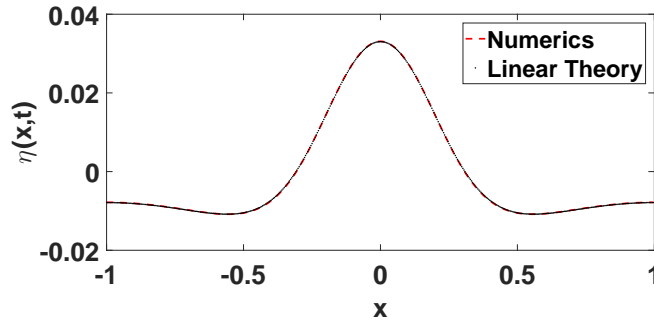
Figure 6: Comparison between linear theory and numerics at $t = .5$ for surface response over two counter-propagating vortices.

To further explore the role of nonlinearity, we now look at longer timescales where we let time $t = 9 \sim 45F$. We truncate the DNO expansions at the

17

18th term, i.e. G_{17}. As seen in Figure 7, comparing the surface profiles at $t = 3$, 6, and 9, higher frequency phenomena and distinguished peaks form as the vortices rise. Looking at the power spectra at $t = 9$ in Figure 8, we see that a significant amount of energy has been transported into higher wave numbers as the vortices rise. As seen in Figure 9, as the vortices rise, the amount of energy shared between the surface and the vortices stays relatively constant up to about $t = 4$. But once high enough, the vortices begin to pump energy into the surface at a greater rate as seen near $t = 9$.

Longer time simulations show that after $t = 9$, the numerical method breaks down with the appearance of ever higher frequency oscillations, which suggests that the wave is near breaking in physical settings. See also Figure 8, where one sees that while high-frequency modes are still at relatively low energies, the surface profile is no longer well sampled. The appearance of these high frequency modes corresponds to a sharp rise in the total surface energy as seen in Figure 9. However, again presumably due to the bottom boundary, as seen in Figure 10, this breaking occurs even though the vortices are still well separated from the surface. Further, we see that the vortices reflect away from the surface near $t = 9$, reminiscent of vortex motion in inviscid wall bounded flow [18].
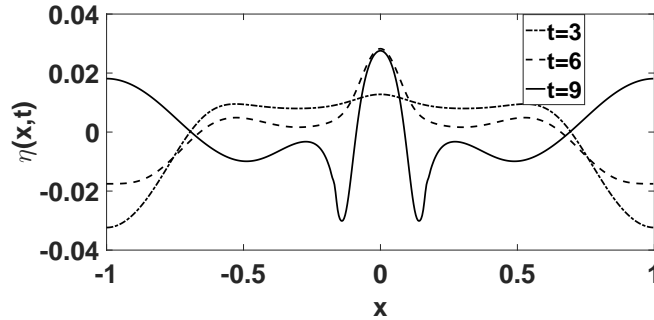
Figure 7: Surface response $\eta(x,t)$ at $t = 3$, $t = 6$, and $t = 9$ over two counter-propagating vortices.

4.3   Four Propagating Vortices: Plus/Plus, Minus/Minus

Using the same numerical scheme and parameters as from above, we now look at the case of four vortices, chosen with vortex strengths

$$\Gamma_1 = \Gamma_2 = 1, \ \Gamma_3 = \Gamma_4 = -1.$$

We refer to this choice of vortex strengths as the 'Plus/Plus, Minus/Minus' case. The Froude number is set to $F = .2$. In this case, the simulation is run to $t_f = 6$, after which higher frequency waves appear in the surface profile signaling the possible onset of wave-breaking. Before this point though, the
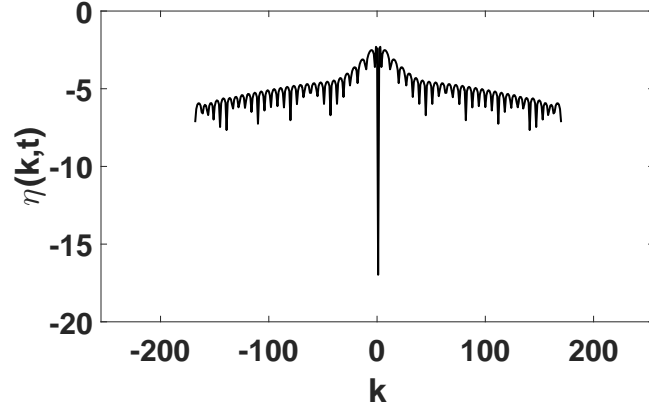
Figure 8: Log plot of the power spectrum at $t = 9$ over wave numbers $-256 \leq k \leq 256$. As can be seen, the rising vortices pump more energy into higher wavenumbers in the surface profile.
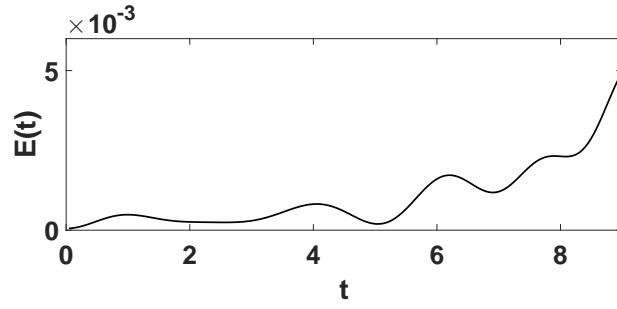

Figure 9: Surface energy profile $E(t)$ for a surface over two vortices for $0 \leq t \leq 9$.
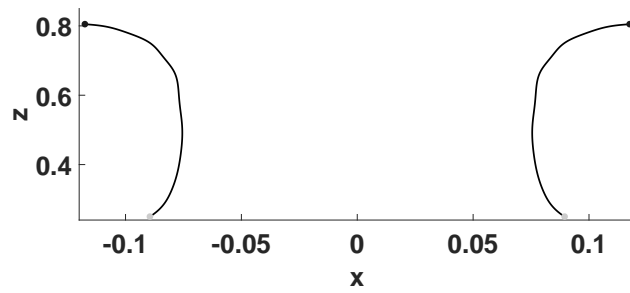

Figure 10: Motion of the two counter-propagating vortices for $0 \leq t \leq 9$. The light grey dots indicate where the vortices begin and the black dots indicate their positions at $t = 9$.

vortices are able to rotate around each other while rising up the fluid column as seen in Figure 12. This likewise produces a prounced central peak in the surface at $t = 6$; see Figure 11. As expected, this also corresponds to a distinct change in the rate of energy input into the surface as seen in Figure 13. This Plus/Plus, Minus/Minus case gives us our first sense of how one might simulate underwater eddies beneath free surface waves.
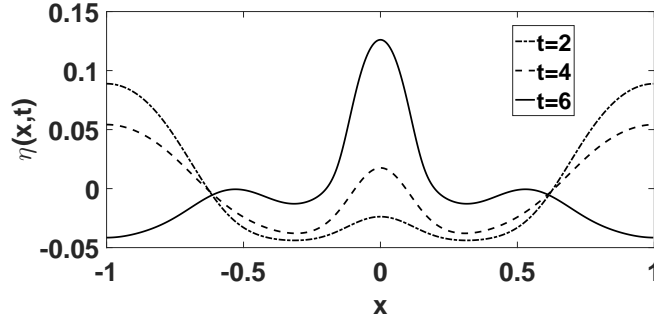
Figure 11: Surface response $\eta(x, t)$ for $t = 2$, 4, and 6 over four vortices in the Plus/Plus, Minus/Minus configuration.
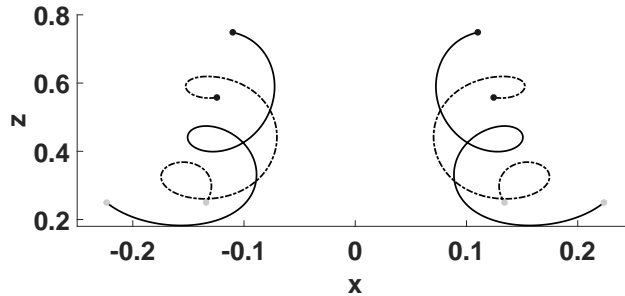
Figure 12: Motion of four vortices in the Plus/Plus, Minus/Minus configuration for $0 \leq t \leq 6$.

4.4 Four Propagating Vortices: Plus/Minus, Minus/Plus

We now examine the case of four vortices with vortex strengths chosen such that

$$\Gamma_1 = 1, \ \Gamma_2 = -1, \ \Gamma_3 = -1, \ \Gamma_4 = 1,$$

which is why we refer to this case as 'Plus/Minus, Minus/Plus'. We choose $F = .2$. The simulation can be run to $t_f = 4$ before high frequency phenomena causes the numerical method to break down. As seen in Figure 14, the surface profile is highly asymmetric. Likewise, it is clear that the peak in Figure 14 is due to the presence of the leftmost vortex pair as seen in Figure
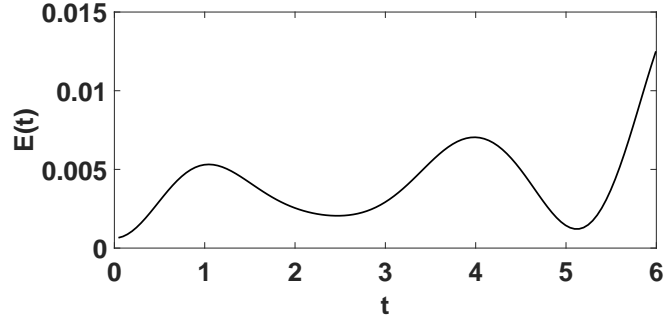
20

Figure 13: Surface energy profile $E(t)$ in response to the motion of four vortices in the Plus/Plus, Minus/Minus configuration for $0 \leq t \leq 6$.

15. The vortex pair on the right side travels down, where it behaves as in inviscid wall-bounded flows [18].
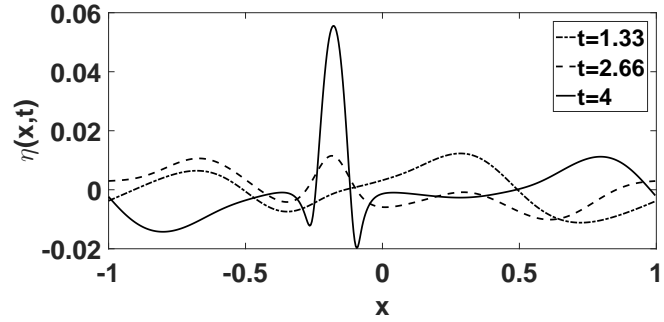

Figure 14: Surface response $\eta(x,t)$ for $t = 1.33, 2.66$, and 4 over four vortices in the Plus/Minus, Minus/Plus configuration.
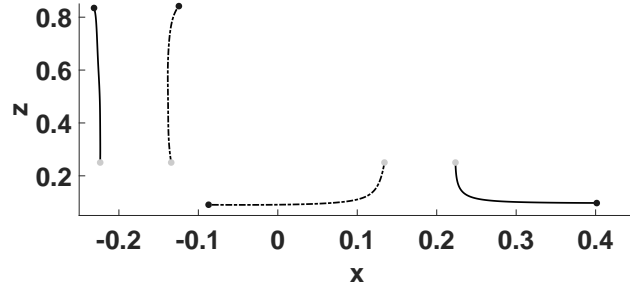

Figure 15: Motion of four vortices in the Plus/Minus,Minus/Plus configuration for $0 \leq t \leq 4$. Note that the leftmost pair of vortices is directly underneath the peak of the surface profile at $t = 4$ as seen in Figure 14.
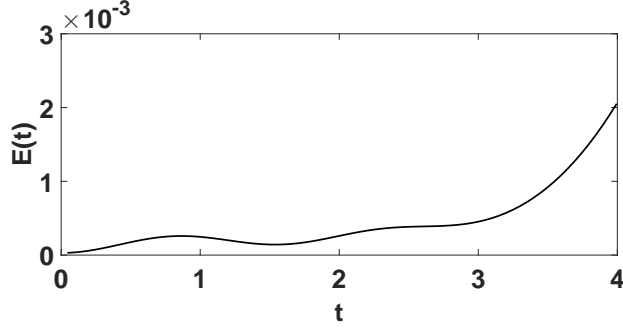
Figure 16: Surface energy profile $E(t)$ in response to the motion of four vortices in the Plus/Minus, Minus/Plus configuration for $0 \leq t \leq 4$.

4.5   Four Propagating Vortices: Plus/Minus,Plus/Minus

Finally, we now look at the case of four vortices, chosen so that

$$\Gamma_1 = 1, \ \Gamma_2 = -1, \ \Gamma_3 = 1, \ \Gamma_4 = -1.$$

The Froude number is again set at $F = .2$. In keeping with our convention, this is called the 'Plus/Minus,Plus/Minus' case. The simulation can be run to $t_f = 4$ before high frequency phenomena causes the numerical method to break down. The flow breaks the symmetry of the vortices in the vertical direction, as seen in Figure 18. Likewise, this case produces perhaps the most distinct and complicated surface profile as seen in Figure 17. Again, the appearance of this more complicated surface profile correpsonds to an increased rate of energy input from the motion of the vortices as seen in Figure 19.
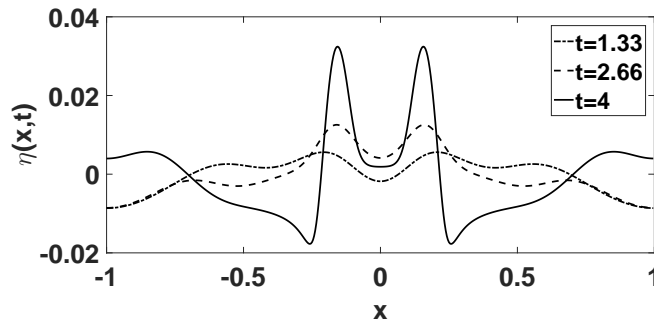

Figure 17: Surface response $\eta(x,t)$ for $t = 1.33$, 2.66, and 4 to four vortices in the Plus/Minus,Plus/Minus configuration.
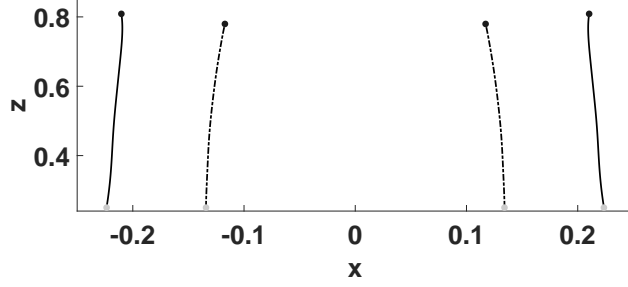
Figure 18: Motion of four vortices in the Plus/Minus,Plus/Minus configuration for $0 \leq t \leq 4$. Note that the peaks at $t = 4$ in the surface profile seen in Figure 17 are directly above the vortices.
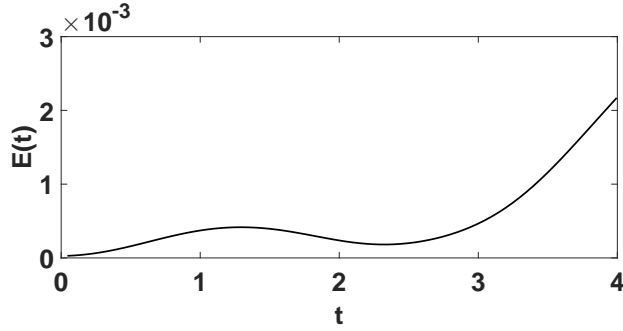

Figure 19: Surface energy profile $E(t)$ in response to the motion of four vortices in the Plus/Minus, Plus/Minus configuration for $0 \leq t \leq 4$.

5   Conclusions and Future Work

In this paper, we have derived a nonlinear integro-differential system of equations in terms of surface variables and vortex positions alone which allows for the ready development of numerical simulations and asymptotic approximations. While being able to recreate known results for two counter-propagating vortices, our approach allows for arbitrary, non-symmetric vortex configurations to be simulated which also take into account the influence of bottom boundaries of the fluid. The presence of bottom boundaries was shown to strongly influence dynamics, leading for example to breaking like phenomena on much shorter time scales than previously reported for deep water flows.

Further, since we allow for more complicated, asymmetric vortex motion, more complicated, and in particular asymmetric, surface profiles were modelled. We likewise have shown a number of potential mechanisms for generating wave breaking, though more sophisticated simulations are necessary to fully study this phenomena. The simulation of interactions between

surface waves and eddies in more complicated fluid environments is a direction of future work which will build off the results in this paper.

References

[1] P.A. Tyvand. On the interaction between a strong vortex pair and a free surface. *Phys. Fluids A*, 2:1624–1634, 1990.

[2] P.A. Tyvand. Motion of a vortex near a free surface. *J. Fluid Mech.*, 225:673–686, 1991.

[3] S. Fish. Vortex dynamics in the presence of free surface waves. *Phys. Fluids A*, 3:504–506, 1991.

[4] D.L. Marcus and S.A. Berger. The interaction between a counter-rotating vortex pair in vertical ascent and a free surface. *Phys. Fluids A*, 1:1988–2000, 1989.

[5] J. G. Telste. Potential flow about two counter-rotating vortices approaching a free surface. *J. Fluid Mech.*, 201:259–278, 1989.

[6] W.W. Willmarth, G. Tryggvason, A. Hirsa, and D. Yu. Vortex pair generation and interaction with a free surface. *Phys. Fluids A*, 1:170–172, 1989.

[7] E.A. Kuznetsov and V.P. Ruban. Cherenkov interaction of vortices with a free surface. *JETP*, 88:492–505, 1999.

[8] M.J. Ablowitz, A.S. Fokas, and Z.H. Musslimani. On a new non-local formulation of water waves. *J. Fluid Mech.*, 562:313–343, 2006.

[9] W. Craig and C. Sulem. Numerical simulation of gravity waves. *J. Comput. Phys.*, 108:73–83, 1993.

[10] P. Guyenne and D.P. Nicholls. A high-order spectral method for nonlinear water waves over moving bottom topography. *SIAM J. Sci. Comput.*, 30:81–101, 2007.

[11] A. Rouhi and J. Wright. Hamiltonian formulation for the motion of vortices in the presence of a free surface for ideal flow. *Phys. Rev. E*, 48:1850–1865, 1993.

[12] C. Lin, T.C. Ho, S.C. Chang, S.C. Hsieh, and K.A. Chang. Vortex shedding induced by a solitary wave propagating over a submerged vertical plate. *Int. J. Heat and Fluid Flow*, 26:894–904, 2005.

[13] K.A. Chang, T.J. Hsu, and P.L.F. Liu. Vortex generation and evolution in water waves propagating over a submerged rectangular obstacle. Part I: Solitary waves. *Coast. Eng.*, 44:13–36, 2001.

[14] K.A. Chang, T.J. Hsu, and P.L.F. Liu. Vortex generation and evolution in water waves propagating over a submerged rectangular obstacle. Part II: Cnoidal waves. *Coast. Eng.*, 52:257–283, 2005.

[15] H. Borluk and H. Kalisch. Particle dynamics in the KdV approximation. *Wave Motion*, 49:691–709, 2012.

[16] A. Nachbin and R. Ribeiro-Junior. A boundary integral formulation for particle trajectories in Stokes waves. *Discrete Contin. Dyn. Syst. Ser. B*, 34:3135–3153, 2014.

[17] G. R. Baker and D. I. Meiron anbd S.A. Orszag. Generalized vortex methods for free-surface flow problems. *J. Fluid. Mech.*, 123,:477–501, 1982.

[18] H. Lamb. *Hydrodynamics*. Dover, New York, N.Y., 1945.